GFZ
Helmholtz-Zentrum
POTSDAM

Originally published as:

Qian, H., Mechie, J., Li, H., Xue, G., Su, H., Cui, X. (2018): Structure of the Crust and Mantle Down to 700 km Depth beneath the Longmenshan From *P* Receiver Functions. - *Tectonics*, *37*, 6, pp. 1688—1708.

DOI: http://doi.org/10.1029/2017TC004726

AGU100 ADVANCING EARTH AND SPACE SCIENCE

Tectonics

RESEARCH ARTICLE
10.1029/2017TC004726

Special Section:
Ten years after the Wenchuan earthquake: new insights into the geodynamics of the eastern Tibet

Structure of the Crust and Mantle Down to 700 km Depth beneath the Longmenshan From *P* Receiver Functions

H. Qian[1], J. Mechie[2], H. Li[1], G. Xue[3], H. Su[3], and X. Cui[1]

[1]Key Laboratory of Continental Dynamics of Ministry of Land and Resources, Institute of Geology, Chinese Academy of Geological Sciences, Beijing, China, [2]Section "Geophysical Deep Sounding", Deutsches GeoForschungsZentrum-GFZ, Potsdam, Germany, [3]Institute of Mineral Resources, Chinese Academy of Geological Sciences, Beijing, China

Abstract Since the Ms 8.0 Wenchuan earthquake occurred in 2008 in the Longmenshan at the eastern margin of Tibet, this region has attracted much attention. In order to investigate the deep structure of the region, an analysis of *P* receiver functions was carried out, using data from an array of 80 broadband seismic stations operated in 2012 and 2013, and straddling the Longmenshan fault zone around the epicenter of the Wenchuan earthquake. Positive *Ps* conversions from 5 to 10 km depth indicate the base of the Mesozoic sediments in the Sichuan basin and the base of the Songpan-Ganzi flysch deposits in Tibet. Later positive *Ps* conversions represent the Moho, which occurs at 40–50 km depth below the Sichuan basin and deepens to the NW to 55–70 km depth under Tibet. An important finding of this study is that whereas in the NE, the Moho deepening from SE to NW is smooth, in the middle and SW of the region the Moho deepening is abrupt with, in some places, a possible overlap. Negative *Ps* conversions at stations in Tibet represent the top of low shear velocity zones in the middle and lower crusts below Tibet. Beneath the Sichuan basin, a negative phase about 1 s earlier than the Moho *Ps* conversion is to a large extent, almost certainly due to multiples from discontinuities in the upper crust. Finally, positive *Ps* conversions can be observed from the 410 and 660-km discontinuities at the top and bottom of the mantle transition zone, respectively.

Key Points:
- The character of Moho deepening from the Sichuan basin to the Tibet plateau is variable along the trend of the Longmenshan fault zone
- In the NE of the study region the Moho deepening is smooth, whereas in the middle and SW the deepening is abrupt
- Where there is an abrupt deepening of the Moho, there are perhaps indications in some cases for a Moho overlap

Supporting Information:
- Supporting Information S1

Correspondence to:
J. Mechie,
jimmy@gfz-potsdam.de

Citation:
Qian, H., Mechie, J., Li, H., Xue, G., Su, H., & Cui, X. (2018). Structure of the crust and mantle down to 700 km depth beneath the Longmenshan from *P* receiver functions. *Tectonics*, *37*, 1688–1708. https://doi.org/10.1029/2017TC004726

Received 19 JUL 2017
Accepted 7 MAY 2018
Accepted article online 21 MAY 2018
Published online 5 JUN 2018

©2018. American Geophysical Union. All Rights Reserved.

1. Introduction and Geology

Since the occurrence of the Ms 8.0 Wenchuan earthquake which ruptured about 300 km of the Longmenshan fault zone in May 2008 (Li et al., 2013), this region at the eastern margin of the Tibetan plateau has attracted the attention of many Earth scientists. Since the earthquake, the Wenchuan Earthquake Fault Scientific Drilling Project has drilled several holes down to 3 km depth (Li et al., 2013). In order to investigate the deep structure of the region surrounding the epicenter of the Wenchuan earthquake and the scientific drilling project, an array of 80 broadband seismic stations in a 300 km × 150 km area straddling the Longmenshan fault zone was operated from June 2012 to October 2013 (Figure 1 and Table S1 in the supporting information). The array was operated by the Chinese Academy of Geological Sciences together with the Deutsches GeoForschungsZentrum Potsdam. While the array was operating the Ms 6.6 Lushan earthquake occurred in April 2013 at the SW edge of the array (Cook et al., 2013; Qian et al., 2016).

The Longmenshan marks the eastern boundary of the Tibetan plateau. Within the study region the Longmenshan is cored by the Pengguan and Baoxing massifs (Figure 1), anticlinal structures exposing Precambrian crystalline rocks (Cook et al., 2013, in which a more detailed description of the geology of the region can be found). The remainder of the range is made up of predominantly Precambrian and Paleozoic rocks. To the northwest of the Longmenshan lies the Songpan-Ganzi terrane, one of the major crustal units of the high Tibetan plateau. This terrane consists predominantly of Triassic rocks of the Songpan-Ganzi flysch, thought to have a thickness generally in excess of 10 km and locally up to 15 km (Weislogel, 2008). To the southeast of the Longmenshan lies the Sichuan basin. From an analysis of industry seismic reflection profiles and velocity data from oil and hydrological wells, Wang et al. (2016) estimate that up to 12–13 km of Precambrian, Paleozoic, Mesozoic, and Quaternary sediments have been deposited in the Sichuan basin in the area of this study. The Quaternary sediments can be up to about 400 m thick where they exist and the Mesozoic sediments have thicknesses of up to about 8 km and compressional (*P*) velocities generally between 4 and 5.6 km/s (Wang et al., 2016). These sediments are underlain by Paleozoic and Precambrian sediments up to about 5 km thick and with *P* velocities in excess of 6 km/s (Wang et al.,

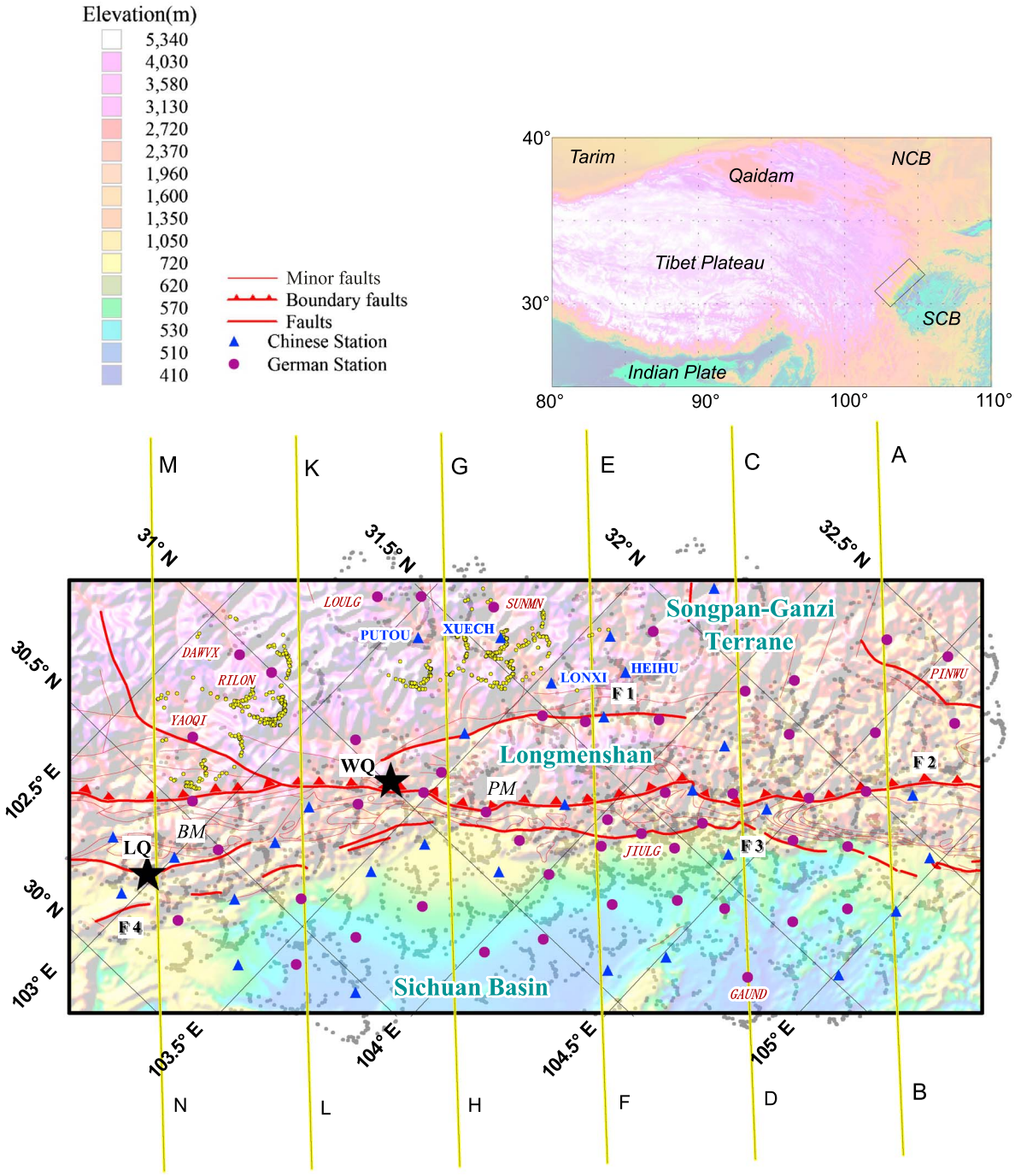

Figure 1. Location map of the Longmenshan area (black rectangle in the small map of the Tibet plateau) showing the distribution of seismic stations deployed during the experiment. The red lines mark the fault systems F1 (Maoxian-Wenchuan Fault), F2 (Yinxiu-Beichuan Fault), F3 (Guanxian-Anxian Fault), and F4 (Guankou Fault) from west to east. The yellow lines mark the locations of the six cross sections for which migrated images are shown. The small gray dots mark the positions of the piercing points of the *P* receiver functions at 55 km depth where only a single Moho conversion is observed. The small yellow dots mark the positions of the piercing points of the *P* receiver functions at 55 km depth from the azimuths of those stations where both upper and lower Moho conversions are observed. The epicenters of the Wenchuan earthquake (WQ) and the Lushan earthquake (LQ) are marked by black stars. Key: NCB, North China Block; SCB, South China Block; PM, Pengguan massif; BM, Baoxing massif.

2016). The Longmenshan is cut by a number of SW-NE trending faults (Figure 1), which together form the Longmenshan fault zone. Of these faults, the major ones in the study area are from west to east, the Maoxian-Wenchuan fault, the Yinxiu-Beichuan fault (YBF), the Guanxian-Anxian fault, and the Guankou fault (F1-F4 in Figure 1). The Wenchuan earthquake caused coseismic rupture along both the Yinxiu-

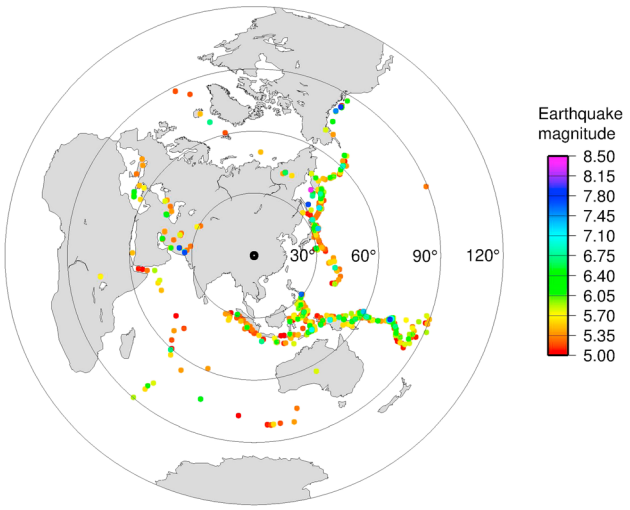

Figure 2. Map showing the distribution of earthquakes (colored dots according to magnitude) used in this study.

Beichuan and Guanxian-Anxian faults, while the Lushan earthquake was located on the Guankou fault (Qian et al., 2016). From Global Positioning System data, present-day convergence across the Longmenshan is relatively small at 4 ± 2 mm/yr (Zhang et al., 2004).

Previous seismological work in the region includes several controlled-source (e.g., Guo et al., 2013; Jia et al., 2014; Wang et al., 2007, 2013, 2015; Xu et al., 2016) and passive-source experiments (e.g., Liu et al., 2014; Robert et al., 2010; Zhang et al., 2009, 2010). The controlled-source experiment of Wang et al. (2007) comprised an E-W trending refraction/wide-angle reflection profile crossing the Longmenshan fault zone at 30°N and thus at the southwestern edge of the array presented in this study. Wang et al. (2015) carried out a NW-SE trending controlled-source, refraction/wide-angle reflection profile crossing the Longmenshan fault zone at about 30.5°N. The controlled-source, refraction/wide-angle reflection experiment of Wang et al. (2013) and one of the passive-source experiments (Zhang et al., 2009, 2010) were carried out along profiles oriented NW-SE and which crossed the Longmenshan fault zone at about 31°N. Jia et al. (2014) carried out a NW-SE trending controlled-source, refraction/wide-angle reflection profile crossing the Longmenshan fault zone at about 31.4°N. A further two controlled-source experiments were a near-vertical incidence reflection profile (Guo et al., 2013) and a refraction/wide-angle reflection profile (Xu et al., 2016) along the same NW-SE trending transect which crossed the Longmenshan fault zone at 31.6°N. The models of Wang et al. (2007), Wang et al. (2013), Jia et al. (2014), Wang et al. (2015), and Xu et al. (2016) from the controlled-source experiments show the sediments of the Sichuan basin thickening southeastward until they reach a thickness of 6–7 km, 30–50 km SE of the Longmenshan fault zone. In view of the study by Wang et al. (2016), it is probable that Wang et al. (2007), Wang et al. (2013), Jia et al. (2014), Wang et al. (2015), and Xu et al. (2016) interpreted the boundary between the Mesozoic and Paleozoic sediments as the interface between the base of the sediments and the top of the crystalline basement under the Sichuan basin. As in the study by Wang et al. (2016), below about 3.5 km depth, the boundary between the Mesozoic and Paleozoic sediments has a *P* velocity contrast of 0.5–1.0 km/s across it and represents the interface between rocks with *P* velocities less than 6 km/s and rocks with *P* velocities greater than 6 km/s, it is perhaps not surprising that Wang et al. (2007), Wang et al. (2013), Jia et al. (2014), Wang et al. (2015), and Xu et al. (2016) interpreted this boundary as the interface between the base of the sediments and the top of the crystalline basement. A further passive-source experiment (Robert et al., 2010) was a profile oriented E-W at about 31°N, where it crossed the Longmenshan fault zone. Yet another passive-source experiment (Liu et al., 2014) comprised an array of almost 300 recording stations in western Sichuan province. As part of their results, Liu et al. (2014) presented the crustal shear (*S*) velocity structure along an E-W cross section at 31°N crossing the Longmenshan fault zone. All of these previous experiments showed that the Moho deepens in going from the Sichuan basin toward the Tibetan plateau. The study of Zhang et al. (2010) also showed an image of the mantle transition zone. A comparison between the Moho and mantle transition zone structures derived from these previous experiments and the structures resulting from this study will be made below.

2. Data Processing and Examples and 1-D Model for the Sichuan Basin

The theoretical background of the *P* receiver function technique used to analyze the waveforms has been described in many publications (see e.g., Ammon et al., 1990; Kind et al., 1995; Langston, 1979; Owens et al., 1984; Vinnik, 1977; Yuan et al., 1997). In this study, the data were recorded continuously at 50 samples per second. From the Advanced National Seismic System and U.S. Geological Survey global earthquake catalogues, 680 teleseismic events with epicentral distances ranging from 30° to 90° and magnitudes greater than or equal to 5.0 were selected (Figure 2). Most of these events occur to the east of the array, but a respectable number also occur to the west (Figure 2). The data for these events were extracted from the continuous data recordings and were processed for the *P* receiver function analysis. In doing so, the Computer Programs in Seismology package by Herrmann and Ammon (2002) was partly utilized. Processing steps included

band-pass filtering from 2 to 20 s and rotation from the coordinate system (vertical, NS horizontal, and EW horizontal) in which the data were recorded to a ray-based (*P*, *SV*, *SH* or L, Q, T) coordinate system (see e.g., Feng et al., 2014; Kind et al., 1995, 2012; Yuan et al., 1997). The rotation angles were obtained from the back azimuth angle for the horizontal angle and the covariance matrix of the vertical and radial components of the *P* wave group for the vertical angle (Kind et al., 1995). In doing so, the best angle of incidence minimizes the *P* wave energy on the *SV* component (Kumar et al., 2006). In the best case, it will eliminate the *P* wave energy on the *SV* component. The next step was an iterative time domain deconvolution of the *SV* component by the *P* component, in which only traces with a signal-to-noise ratio greater than 1.5 were accepted and deconvolved. Noise was defined from 70 s before the onset time of the first *P* wave to the onset time of the first *P* wave, while signal was defined as the first 160 s following the onset time of the first *P* wave. Following the deconvolution a further automatic selection for good quality traces was carried out, involving two steps. First, receiver functions with anomalously large peaks in the *P* wave coda were discarded. Second, a comparison with the final stacked receiver function for the respective station was carried out and the trace was only accepted if the correlation coefficient was greater than 0.25. Finally, each individual receiver function was visually inspected and traces with no *P* to *S* (*Ps*) conversion at the Moho or with strong low-frequency oscillations were omitted, which resulted in 11,204 suitable *P* receiver functions. For summation of many traces in the time domain, a distance moveout correction with respect to a reference epicentral distance of 67° (reference slowness of 6.4 s per degree) was performed (Yuan et al., 1997), using a simplified version of the IASP91 velocity model (Kennett & Engdahl, 1991), with the Moho at 65 km depth. For stations in the Sichuan basin the distance moveout correction was also applied, for purposes of comparison, with the Moho at 47 km depth. The differences are minimal (cf. Figures 3a and S1 in the supporting information).

Examples of *P* receiver functions obtained for the stations GAUND and LOULG on either side of the Longmenshan fault zone (Figure 1) are presented (Figure 3). The station GAUND is located east of the Longmenshan fault zone on Mesozoic rocks in the Sichuan basin at an elevation of about 430 m. One of the most prominent signals is the positive *Ps* conversion, indicating a velocity increase with depth, at 5 to 6-s delay time (M in Figures 3a and S1). It can be recognized on many individual traces and is prominent in the summed trace at the top. It represents the conversion from the Moho which would then imply a crustal thickness of 40–48 km. Another significant signal is a negative pulse at 4 to 5-s delay time (N in Figures 3a and S1). It is prominent in both the individual traces and the summed trace at the top. It occurs about 1 s earlier than the Moho conversion, and the same is true in the case of traces without the moveout correction applied (Figure 3b). It is possible that this phase is a multiple from the sediments in the Sichuan basin. It is also possible that it represents the conversion from the top of a low velocity zone (LVZ) about 10 km above the Moho. It could also be a combination of these two possibilities. Due to the fact that the expected moveouts are small, being about −0.25 s between 30° and 90° distance in the case of a primary *Ps* conversion from the top of a lower crustal LVZ and just 0.06 s between 30° and 90° distance in the case of the *PpSs* multiple from the sediments, it is difficult to distinguish, based on the moveout, between the two possibilities. The station LOULG is located west of the Longmenshan fault zone in the Songpan-Ganzi terrane of the high Tibetan plateau at an elevation of about 2,270 m. For this station, positive *Ps* conversions from the Moho can be observed at about 8 s, indicating a crustal thickness of about 65 km (M in Figure 3c). As in the case of the station GAUND a negative signal is prominent in both the individual traces and the summed trace at the top (N2 in Figure 3c). It has a delay time of 3–4 s. If it is a primary *Ps* conversion, then it indicates the top of a LVZ at 24–32 km depth. Additionally, a second negative signal (N in Figure 3c) can be recognized on some traces between the negative signal, N2, and the Moho. However, due to interference effects from other phases, sometimes with opposite polarity, in the same time range, the negative signal, N does not show up in the summed trace at the top. Finally, a positive *Ps* conversion can be observed at about 1-s delay time in the records for both stations (S in Figure 3). In the case of the station GAUND, situated on Mesozoic rocks in the Sichuan basin, this conversion probably marks the base of the Mesozoic sediments, based on the results of the study by Wang et al. (2016). In the case of the station LOULG on the high plateau, this conversion probably marks the base of the Songpan-Ganzi flysch deposits. At station GAUND the conversion actually occurs at 1.48 s in the summed trace at the top. For the velocity structure in the vicinity of GAUND (Figure 4a and Wang et al., 2016), the conversion time of 1.48 s corresponds to a depth of 9.5 km, which is within 0.8 km of the depth of the base of the Mesozoic sediments according to Wang et al. (2016). The estimated time of the *PpSs* multiple would then be about 7.8 s for a ray parameter of 0.05675 s/km. This is 3.2 s later than

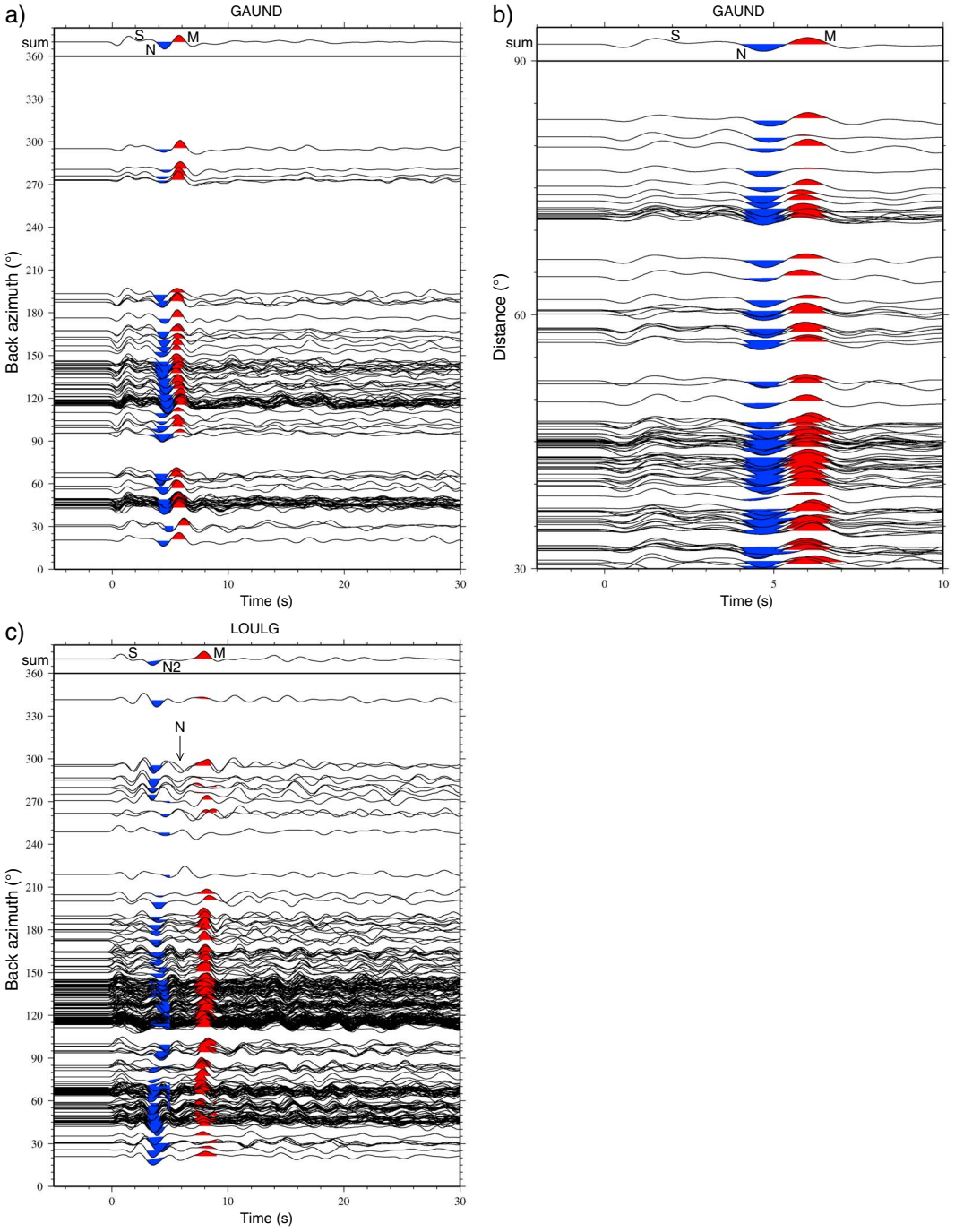

Figure 3. Examples of *P* receiver functions from two stations (a and b) GAUND, east of the Longmenshan fault zone in the Sichuan basin, and (c) LOULG, west of the Longmenshan fault zone on the high Tibetan plateau. The traces have been band-pass filtered from 2 to 20 s and are plotted with moveout correction and according to the back azimuth in the case of (a) and (c) and without moveout correction and according to the distance in the case of (b). The summed trace is shown on the top. For both stations the Moho (red signal marked M), a negative phase (blue signal marked N in the case of GAUND and N2 in the case of LOULG) between 3 and 5-s delay time and a positive *Ps* conversion at about 1-s delay time (marked S) can be clearly seen. In the case of LOULG a further negative phase (marked N) can sometimes be recognized between N2 and M. In this figure the moveout correction has been applied for a Moho depth of 65 km. In Figure S1 the moveout correction is shown for a Moho depth of 47 km for station GAUND.

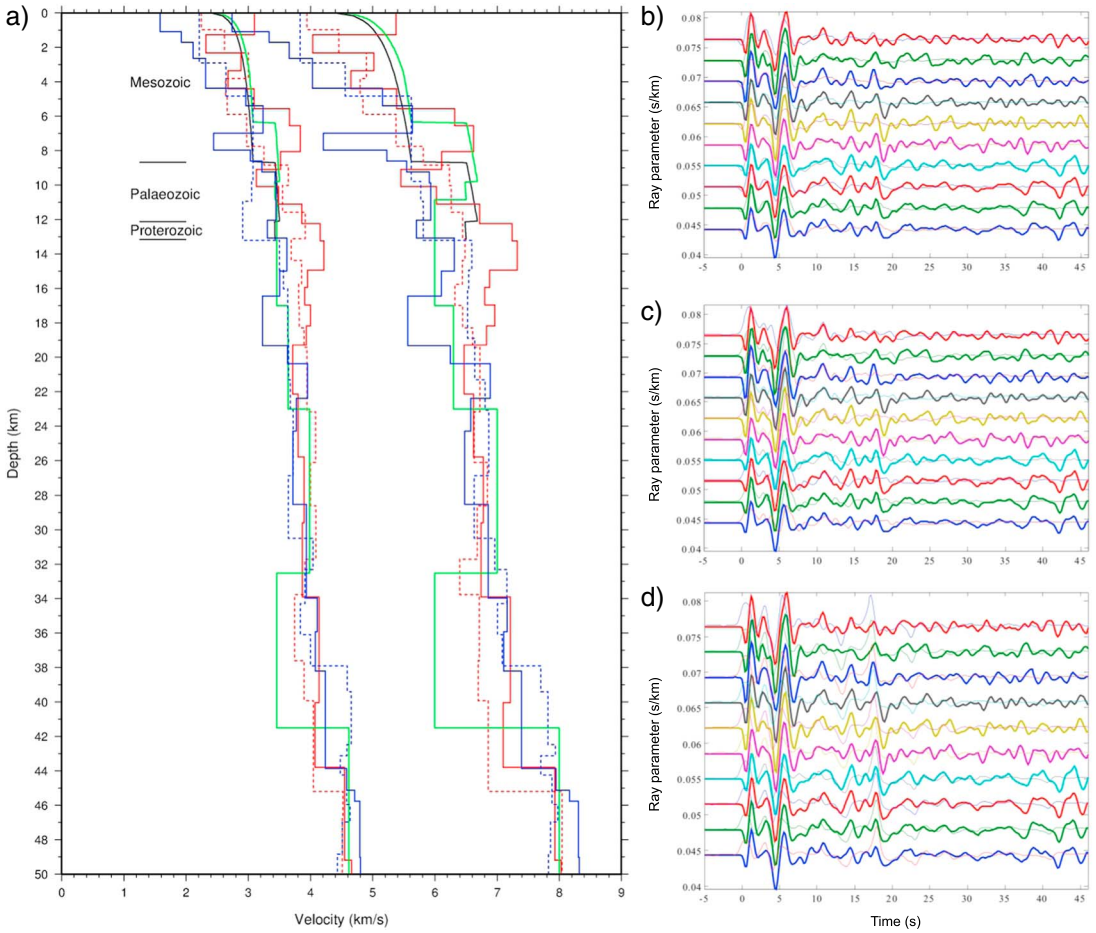

Figure 4. (a) Compressional (*P*) and shear (*S*) velocity-depth functions for station GAUND in the Sichuan basin and (b–d) comparison between observed (thick lines) and theoretical (thin lines) receiver functions for the velocity-depth functions shown in (a). The black lines in (a) show the *P* and *S* velocity-depth functions from Wang et al. (2016), based on an analysis of industry seismic reflection profiles and velocity data from oil and hydrological wells. The full red lines in (a) show the *P* and *S* velocity-depth functions derived from an inversion of the receiver function data and including significant low velocity zones in the top 5 km. The corresponding theoretical receiver functions are shown in (b). The full blue lines in (a) show the *P* and *S* velocity-depth functions derived from an inversion of the receiver function data and including significant low velocity zones at 7–20 km depth. The corresponding theoretical receiver functions are shown in (c). In these two cases, the negative phase at 4–5 s is almost wholly due to structure in the top 20 km of the crust. The dashed red and blue lines in (a) show the initial *P* and *S* velocity-depth functions for the inversions which led to the *P* and *S* velocity-depth functions shown by the full red and blue lines, respectively. The green lines in (a) show the *P* and *S* velocity-depth functions with a significant low velocity zone for *S* waves, only in the lower crust. The corresponding theoretical receiver functions are shown in (d). In this case, the negative phase at 4–5 s is partly due to a multiple from the base of the Mesozoic sediments at about 6.3 km depth and partly to a primary *Ps* conversion from the top of the lower crustal low velocity zone at 32.5 km depth.

the observed negative phase, N, at GAUND. This constitutes additional evidence that the observed negative phase, N, at GAUND is not a multiple from the base of the Mesozoic sediments because the delay time of the phase is wrong. One caveat could be that the observed negative phase, N, is a *PpSs* multiple from a boundary within the Mesozoic sediments for which the primary *Ps* conversion is not observed as a clear separate phase but could contribute energy to the observed phase at about 1.5 s. Another caveat could be that the depth to the base of the Mesozoic sediments is smaller than that provided by Wang et al. (2016) and that the observed phase at about 1.5 s is a mixture of the *Ps* conversion from the base of the Mesozoic sediments and a multiple from a boundary within the Mesozoic sediments.

In an attempt to discriminate between the various possibilities giving rise to the observed negative phase, N, at GAUND and other stations within the Sichuan basin, attempts were made to find velocity-depth functions producing theoretical receiver functions similar to the observed receiver functions. The reflectivity method (Müller, 1985) was used to calculate theoretical seismograms for the velocity-depth functions. Then the theoretical seismograms were rotated into the same ray-based (*P*, *SV*, *SH* or L, Q, T) coordinate system as for the

observed data, deconvolved in the frequency domain, and finally transformed into the time domain to create theoretical receiver functions. The observed traces were stacked in bin sizes of 0.0036 s/km after moveout correction to the same reference ray parameter. Then the moveout correction was removed from the stacked trace and the inversion was carried out. The optimal parameters for a model were determined by iteratively minimizing the mean square deviation between the observed and the theoretical traces generated by the model (see e.g., Coleman & Li, 1994; Kind et al., 1995). In a first step, a velocity-depth function was inverted for, from an initial model (Figure 4a, dashed red lines), with the only constraint being that the ratio of the *P* velocity to the *S* velocity should be 1.72–1.74. This produced a velocity-depth function with significant velocity contrasts including significant LVZs in the upper 5 km (Figure 4a, full red lines) and, in fact, all the way down to about 20 km depth. It produced no significant LVZs in the lower crust. Of the three models tested, this model produced the best fit between observed and theoretical receiver functions (Figure 4b). It implies a thickness of the Mesozoic sediments of 5.5 km (Figure 4a, full red lines), as this is the depth where the velocities increase from values more typical of the Mesozoic sediments to values more typical of the Paleozoic sediments. However, one of the drawbacks of this model is that it does not seem to agree with the velocity-depth function provided for the vicinity of GAUND by Wang et al. (2016) from industry seismic reflection profiles and velocity data from oil and hydrological wells in the Sichuan basin (Figure 4a, black lines). This velocity-depth function shows no significant LVZs in the sedimentary succession. Although the borehole velocity data show considerable small-scale velocity variations and the standard deviations of the *P* velocities can be up to ±0.85 km/s (Wang et al., 2016), there is little indication in the borehole velocity data for the sort of velocity variations on the kilometer scale as in the velocity-depth function derived from the receiver function data. Thus, another model was inverted for, from an initial model (Figure 4a, dashed blue lines), with the additional constraint that there should be no LVZ in the upper 5 km (Figure 4a, full blue lines), which is the depth range covered by the borehole velocity data. This resulted in a velocity-depth function with significant velocity contrasts in the upper 20 km, including significant LVZs between 7 and 20 km depth. However, it also produced no significant LVZs in the lower crust. The fit between observed and theoretical receiver functions (Figure 4c) produced by this model is also quite acceptable, but the theoretical data do not fit the first 2 s of the observed data as well as the previous model. Further, the *P* and *S* velocities in the top 4 km are considerably lower than those provided for the vicinity of GAUND by Wang et al. (2016). The third model has a significant LVZ as the basal crustal layer and has no other significant low *S* velocity zone (Figure 4a, green lines). In this case about 50% of the amplitude of the negative phase, N, at 4 to 5-s delay time is produced by the *Ps* conversion from the upper boundary of the lower crustal LVZ, while the other 50% is produced by the *PpSs* multiple from the significant velocity contrast at 6–7 km depth. It should be noted that the negative phase, N, at 4 to 5-s delay time is very unlikely to be produced only by the *Ps* conversion from the upper boundary of the lower crustal LVZ. If this were to be the case, then this would mean that material with essentially mantle velocity should exist immediately above the LVZ to produce a *Ps* conversion that is essentially the same size as that from the Moho. Although the fit between observed and theoretical receiver functions (Figure 4d) for this model is quite good for the negative phase, N, and the following Moho conversion, it is not as good as that of the first model in the first 2 s. Additionally, this model produces a multiple at 16–19 s which is significantly larger than in the observed data. One reason for the extremely large synthetic multiple is that it is due partly to the *PpPs* multiple from the Moho and partly to the *PpSs* multiple from the top of the lower crustal LVZ. The absence of such a prominent multiple in the observed data is an argument against a lower crustal LVZ. However, it could be possible that the multiples are destroyed by crustal heterogeneities, due to the longer distances traveled by the multiples through the crust, as opposed to the primary *Ps* conversions. Other variants of the above three model types were also tried, but without any greater success. In summary, it would thus seem that all of the models tested have their problems to match both the observed receiver functions and the known velocity information concerning the Sichuan basin as provided by Wang et al. (2016).

3. Imaging, Including Further Data Examples

A time to depth migration of the *P* receiver functions has been carried out (Figure 5 and Table S1). For this purpose a backward propagation along the ray (Yuan, 2000) modified to account for the station elevation and the near-station raypath differences was utilized. The backward propagation along the ray was carried out using ray-tracing through the same simplified version of the IASP91 velocity model (Kennett & Engdahl, 1991) as was used above, with *P* and *S* velocities at the surface of 5.2 and 3.2 km/s, respectively

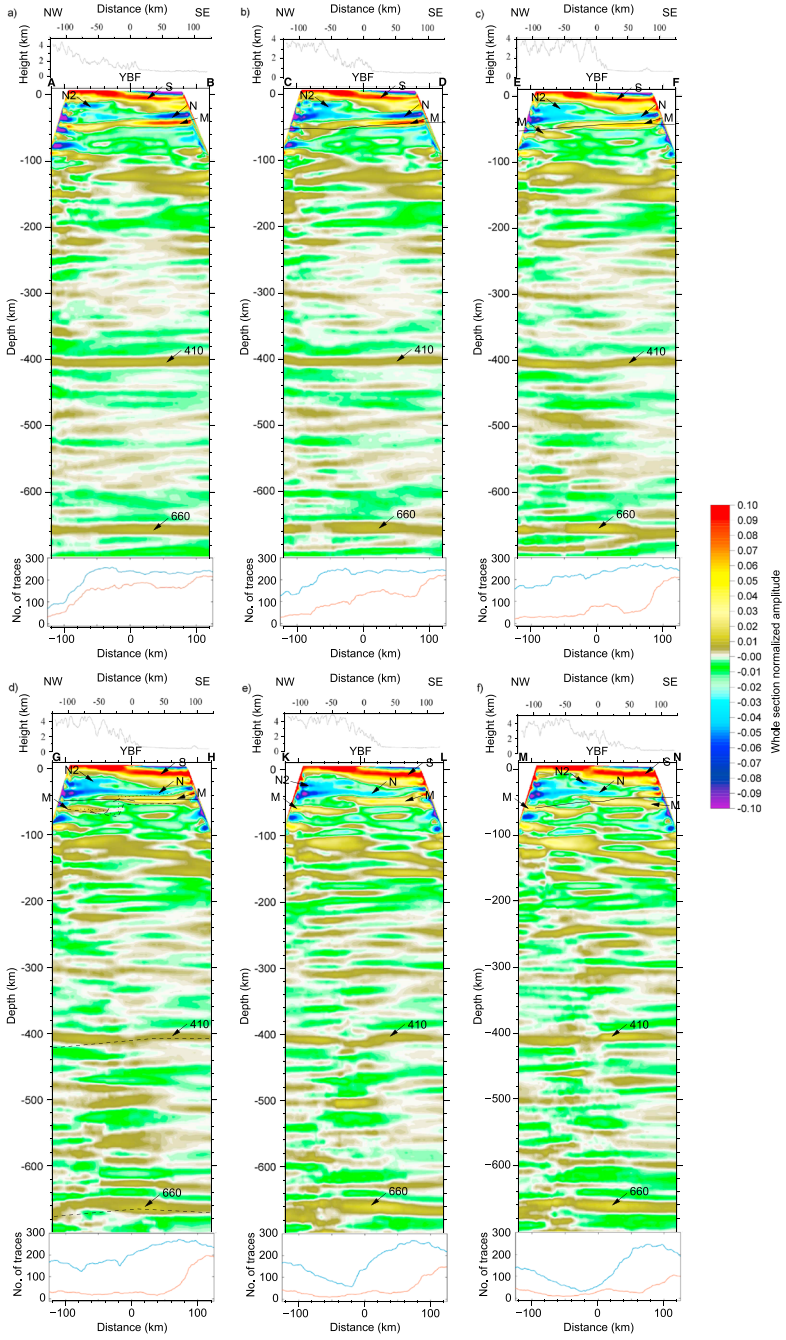

Figure 5. Depth migration images for frequencies up to 0.5 Hz for six cross sections (a) A-B, (b) C-D, (c) E-F, (d) G-H, (e) K-L, and (f) M-N (see Figure 1 for locations). In the migrated images 0 km depth is at mean sea level. Elevation profile is shown above each of the migrated images. The number of traces contributing to the images in the profile direction at 410 km depth (blue line) and 660 km depth (red line) is shown below each of the migrated images. The position of the Yinxiu-Beichuan Fault (YBF, F2 in Figure 1), the major fault in the Longmenshan fault zone in the study area, is also marked above each of the migrated images. In (b) the location of the Moho from Xu et al. (2016) is shown as a black line. In (c) the location of the Moho from Jia et al. (2014) is shown as a black line. In (d) the locations of the Moho from Wang et al. (2013), Robert et al. (2010), Zhang et al. (2010), and Liu et al. (2014) are shown as full, long dashed, short dashed, and dotted black lines, respectively, and the locations of the 410 and 660-km discontinuities from Zhang et al. (2010) are shown as short dashed black lines. In (f) the location of the Moho from Wang et al. (2015) is shown as a black line. Key: S, base of Mesozoic sediments SE of YBF beneath the Sichuan basin and base of Songpan-Ganzi flysch deposits NW of YBF below the Tibetan plateau; N2, top of midcrustal low velocity zone; N, upper crustal multiples and perhaps top of lower crustal low velocity zone SE of YBF and top of lower crustal low velocity zone NW of YBF; M, Moho; 410, 410 km discontinuity; 660, 660 km discontinuity.

(cf. Figure 4a) and with the Moho at 65 km depth. This is an appropriate depth for the stations on the Tibetan plateau (Figure 3c) but is considerably larger than the Moho depth for stations in the Sichuan basin (Figure 3a). Thus, for comparison, a migration was also carried out with the Moho at 47 km depth (Figure S2). There is little difference between the two migrations, and all the features recognized and interpreted in this study look similar in both migrations. The maximum difference in Moho depths between the two migrations does not exceed 3.5 km. The migration method used in this study is similar to the common conversion point method of Dueker and Sheehan (1997, 1998). First, migration was carried out along the event-receiver back azimuth and the amplitudes for specific depths were entered into boxes in a 3-D volume. At crustal and uppermost mantle depths, these boxes were 24 km long in the profile direction, 50 km wide perpendicular to and on either side of the profiles, and 6 km in depth. At 400–700 km depth, the box size was increased to 50–70 km length in the profile direction and 8–10 km in depth. Once all the rays were traced and the respective boxes filled, the amplitudes were normalized by dividing by the number of traces contributing to the total amplitude in each box. This means that the individual receiver functions are reweighted to a certain extent. Receiver functions from the same back azimuth and distance are downweighted as they contribute to the amplitudes in the same boxes with many trace hits and receiver functions from poorly covered back azimuth and distance ranges are upweighted when they contribute to the amplitudes in boxes with only a small number of trace hits. Last, the data were interpolated to produce the final images shown (Figure 5). For comparison, Zhang et al. (2010) used a smoothing operator 60 km long in the horizontal direction and 5 km long in the vertical direction in producing their migration images.

In the present study, the box size used in the migration effectively determines the resolution of the images. For the lateral resolution, the Fresnel zone is generally taken as an appropriate measure on unmigrated data (Sheriff & Geldart, 1995; Yilmaz, 1987). However, migration decreases the size of the Fresnel zone, down to the wavelength in the best cases, and thus improves the lateral resolution (Yilmaz, 1987). Taking the average whole-crustal shear velocity as 3.65 km/s (see below and Wang et al., 2013) and the frequency as 0.5 Hz, the horizontal box size of 24 km utilized at crustal depths is approximately the same size as the radius of the Fresnel zone at the Moho in this study (Sheriff & Geldart, 1995). The threshold for the vertical resolution is generally taken as a quarter of the wavelength (Sheriff & Geldart, 1995; Yilmaz, 1987), which for this study is about 2 km. However, the vertical box size of 6 km utilized at crustal depths is larger than this and, in fact, closer to the wavelength, which is about 7.5 km. Similar arguments apply for the mantle transition zone where, as mentioned above, the box size for the migration was increased.

The bootstrap method was applied in order to provide a measure for the robustness of the depth migration method described above and also to calculate standard deviations for the migration images. This involved randomly sampling the receiver functions with replacement to obtain a bootstrap sample following Sacchi (1998). A migration image was then derived from this bootstrap sample as described above. This procedure was repeated 50 times, and then the average and standard deviation at each point of the images were calculated. The resulting average migration images and standard deviations are shown for the top 100 km (Figure 6) and the mantle transition zone (Figure 7) along the six cross sections. The images of the top 100 km show that the standard deviations are almost always below 0.01 beneath the central portions of the cross sections (Figure 6). The southwesternmost cross section has the highest uncertainties in the central part, just NW of the YBF (Figure 6f). All the features in the top 100 km that are interpreted below to be significant have absolute amplitudes that are greater than 0.02 and thus are larger than twice the standard deviation. The images of the mantle transition zone also show small standard deviations below 0.01 for the two northeasternmost cross sections (Figures 7a and 7b). Toward the SW this remains true for the depth range of the 410-km discontinuity, with the exception of the portion NW of the YBF beneath the southwesternmost cross section (Figure 7f). In contrast, for the depth range of the 660-km discontinuity, the standard deviations beneath the four southwesternmost cross sections increase to between 0.01 and 0.02. There is a correlation between the standard deviations in the mantle transition zone and the number of traces contributing to the images of the 410 and 660-km discontinuities (Figure 5). The larger the standard deviation, the smaller the number of traces is, contributing to the images of the 410 and 660-km discontinuities. The reason that the number of traces contributing to the image of the 660-km discontinuity is generally smaller than the number contributing to the image of the 410-km discontinuity is that the piercing points for the 660-km discontinuity are a greater horizontal distance away from a station than the piercing points for the 410-km

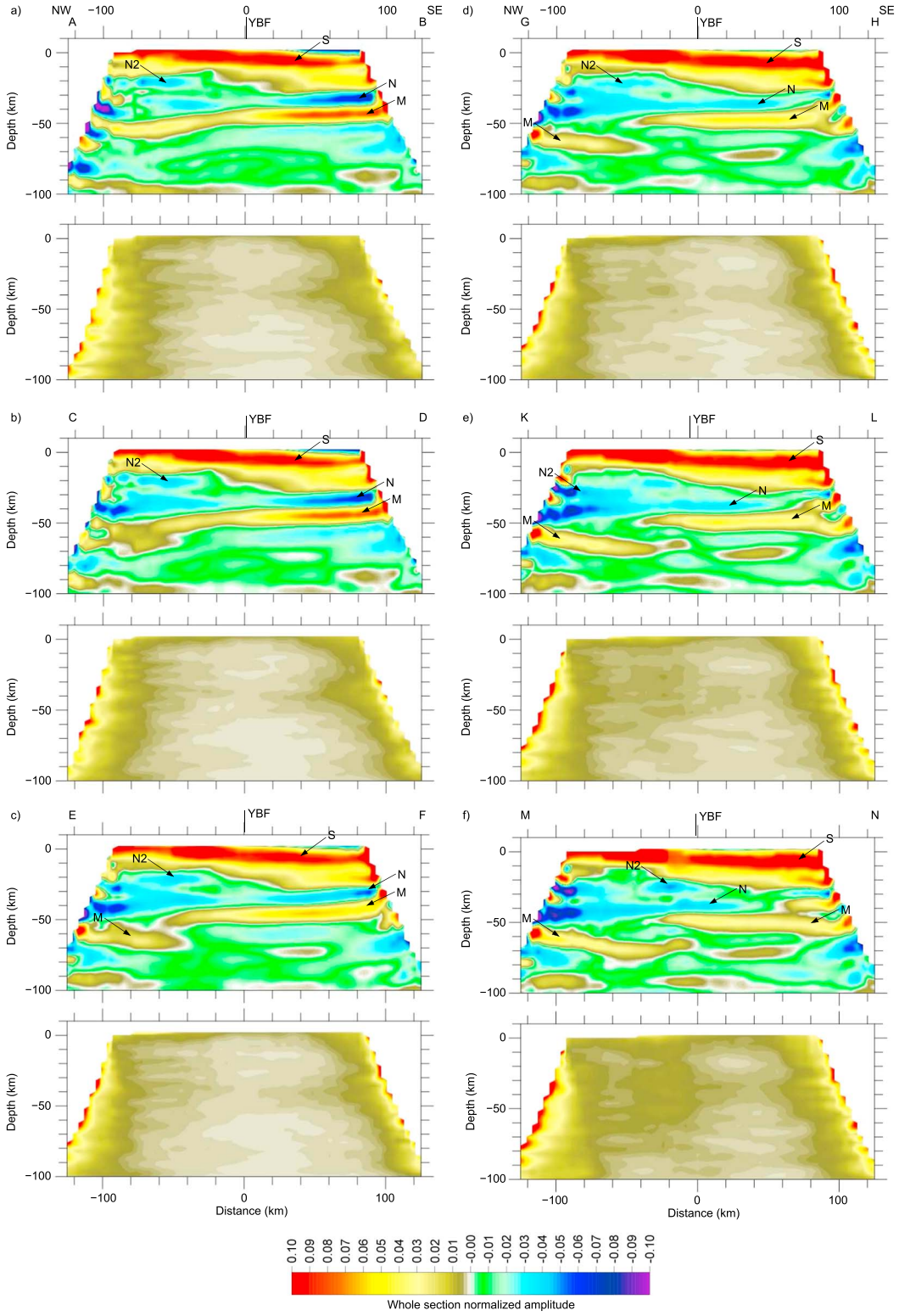

Figure 6. Enlarged images of the top 100 km for the six cross sections (a) A-B, (b) C-D, (c) E-F, (d) G-H, (e) K-L, and (f) M-N shown in Figure 5. In each case, the upper image shows the average and the lower image shows the standard deviation of 50 depth migrations obtained using the bootstrap method with replacement. Key: See Figure 5.

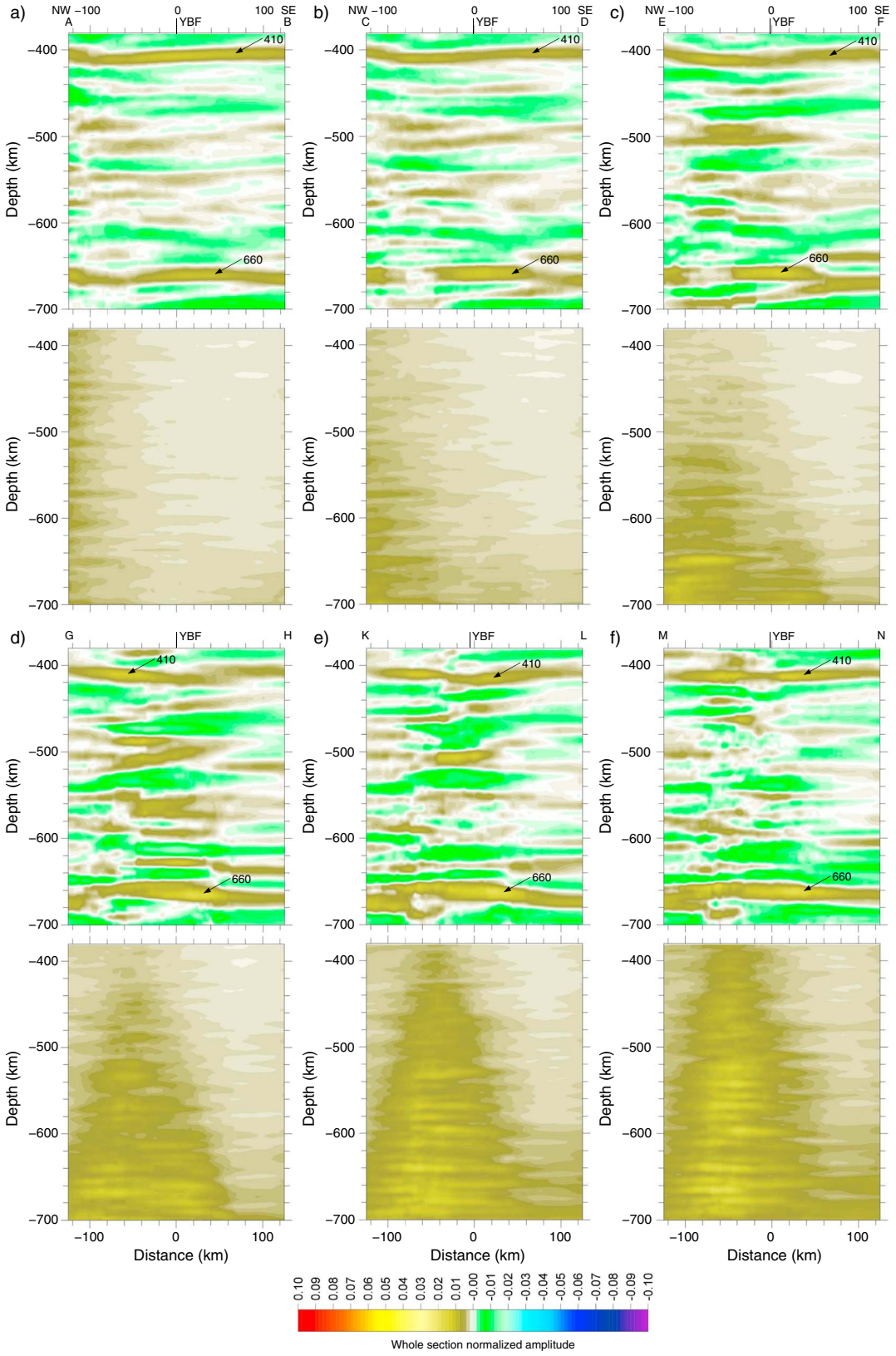

Figure 7. Images of the mantle transition zone for the six cross sections (a) A-B, (b) C-D, (c) E-F, (d) G-H, (e) K-L, and (f) M-N shown in Figure 5. In each case, the upper image shows the average and the lower image shows the standard deviation of 50 depth migrations obtained using the bootstrap method with replacement. Key: See Figure 5.

discontinuity. Thus, fewer piercing points for the 660-km discontinuity fall within the region covered by the migration boxes. This problem is greater for the southwestern cross sections, for example, M-N, as there are fewer events from the southwest (see Figure 2). Thus, while features associated with the 410-km discontinuity can generally be interpreted with some confidence, caution should be exercised when interpreting features associated with the 660-km discontinuity.

In the depth domain images (Figures 5 and 6) the Moho can be well recognized at 40–70 km depth. In all the images the Moho is shallower at the SE end of the cross section beneath the Sichuan basin and deeper at the NW end of the cross section beneath the high Tibetan plateau. However, there is a change in the way that the Moho deepens as one proceeds along the Longmenshan fault zone from NE to SW. Along the two northeastern cross sections (Figures 6a and 6b) the Moho deepens smoothly and gradually from SE to NW, whereas along the four southwestern cross sections (Figures 6c–6f), the Moho deepens abruptly in a step-like manner. In fact, in the three cross sections E-F, K-L, and M-N (Figures 6c, 6e, and 6f) there seems to be some overlap of the deeper Moho from the NW below the shallower Moho from the SE. Only in the cross section G-H, which crosses the Longmenshan fault zone at 31°N, there seems to be only an abrupt step in the Moho, but no overlap (Figure 6d). The overlap in the three cross sections E-F, K-L, and M-N, however, could be artificially exaggerated as the migration boxes have dimensions of 24 and 100 km, perpendicular and parallel to the trend of the Longmenshan, respectively. For this reason a migration was performed in which the box size in the profile direction was reduced from 24 to 12 km (Figures S3g–S3l). Based on the interpretation of the southern extent of the deeper Moho from the NW and the northern extent of the shallower Moho from the SE, it would appear that on some of the cross sections the Moho overlap is about 40 km (Figures S3k and S3l) and thus about 3 times larger than the dimension of the migration box in the profile direction. Thus, it would appear that the Moho overlap could be real, at least in the case of the two southwestern cross sections K-L and M-N (Figures S3k and S3l). The abrupt step in the Moho does not occur more or less below the Longmenshan fault zone but rather occurs up to about 50 km to the NW of the fault zone beneath the high Tibetan plateau (Figures 5c and 6c).

If there is overlap of the deeper Moho from the NW below the shallower Moho from the SE in three of the cross sections, then this implies that there should be some crustal material in the region of the overlap in order to produce the impedance contrast giving rise to the deeper positive *Ps* conversion. This, in turn, implies that there should be a negative *Ps* conversion between the two positive *Ps* conversions as one goes from the mantle material below the upper Moho to the crustal material above the lower Moho. Looking carefully at the three cross sections (Figures 6c, 6e, and 6f), one can see evidence of a negative *Ps* conversion in the region of overlap between the shallower Moho from the SE and the deeper Moho from the NW in the southwesternmost cross section (Figure 6f). Here in the image derived using the bootstrap method, the amplitude of the negative *Ps* conversion is almost −0.03, while the standard deviation is around 0.01. Indications for the overlap of the deeper Moho from the NW below the shallower Moho from the SE can also be seen in the data from some individual stations, for example, station XUECH (Figure 8a) or stations YAOQI, RILON, SUNMN, DAWVX, PUTOU, LONXI, and HEIHU (Figures S4 and S5) situated NW of the YBF (Figure 1). In the data from the station XUECH the shallower Moho can be observed primarily from southeastern azimuths and the *Ps* conversion associated with it occurs at about 6 s delay time in the summed trace at the top (Mu in Figure 8a). The energy from this *Ps* conversion at the station XUECH migrates to positions that are continuous with and at the northwestern end of the shallower Moho from the SE. This lends credibility to the hypothesis that the restricted azimuthal presence of the phase in the data from the station XUECH is, in fact, due to the shallower Moho from the SE terminating in the vicinity of the station XUECH, rather than the presence of anisotropic and/or dipping layer effects (see e.g., Schulte-Pelkum & Mahan, 2014 for a description of anisotropic and/or dipping layer effects). The deeper Moho can be observed from a larger range of azimuths and the *Ps* conversion associated with it occurs at about 8-s delay time in the summed trace at the top (Ml in Figure 8a). Between the two positive peaks a small negative peak occurs in the summed trace at the top. In the individual traces, it can be predominantly observed from southeastern azimuths. In contrast, the data from the station PINWU (Figure 8b), situated in the northeastern part of the array about 45 km NW of the YBF (Figure 1), show a single *Ps* conversion from the Moho at 6.5 to 7-s delay time in the summed trace at the top. This station is situated in the region where the Moho deepens smoothly and gradually from SE to NW (Figures 6a and 6b).

Due to the rather complicated structure in the Moho, it was thought important to obtain some idea about the uncertainties in Moho depths. As alluded to above, this question was partly examined by performing

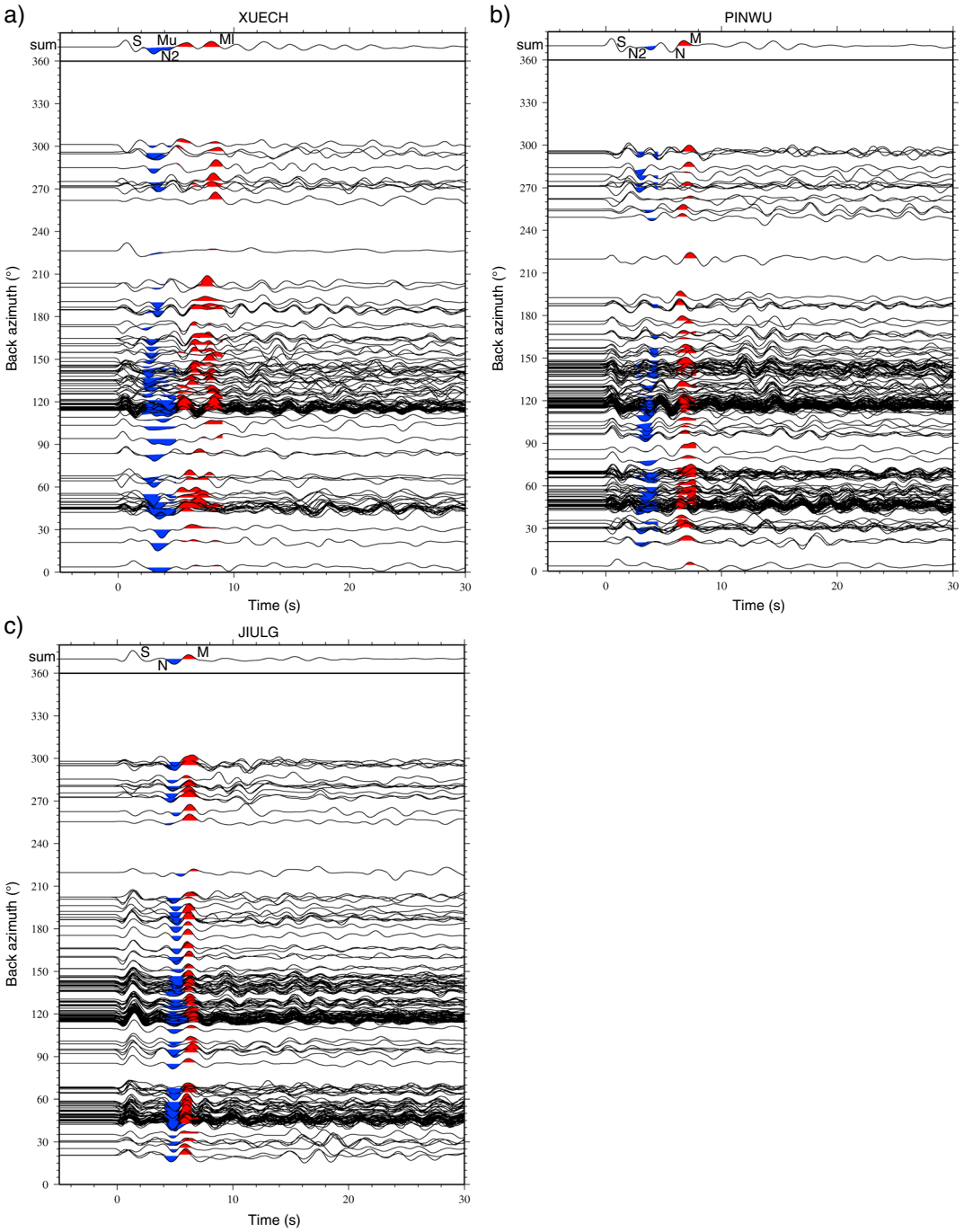

Figure 8. Examples of moveout corrected *P* receiver functions from stations (a) XUECH, (b) PINWU, and (c) JIULG. The traces have been band-pass filtered from 2 to 20 s and are plotted according to the back azimuth. The summed trace is shown on the top. In the case of station XUECH, *Ps* conversions from both an upper Moho (Mu) at about 6-s delay time and a lower Moho (Ml) at about 8-s delay time have been identified, whereas for station PINWU only one *Ps* conversion from the Moho (M) at 6.5 to 7-s delay time has been recognized. For stations XUECH and PINWU, phases S, N2, and N are as described for station LOULG in Figure 3c. For station JIULG, phases S, N, and M are as described for station GAUND in Figures 3a and 3b.

migrations for velocity models with two different Moho depths. One model had a Moho depth of 65 km, appropriate for stations on the Tibetan plateau (Figure 3c), whereas the other model had a Moho depth of 47 km, appropriate for stations in the Sichuan basin (Figure 3a). As noted above, the maximum difference in Moho depths between the two migrations does not exceed 3.5 km (cf. Figures 5 and S2). Further, as the

profiles extend from the Sichuan sedimentary basin through the Longmenshan where crystalline basement is exposed to the Triassic flysch basin in the Songpan-Ganzi terrane of the Tibetan plateau, an attempt was made to estimate the effects of laterally varying crustal velocity structure on Moho depths. The effects of laterally varying crustal velocity structure also include the effects of crustal LVZs. The average whole-crustal shear velocity for the Sichuan basin is 3.6 km/s, whereas that for the Songpan-Ganzi terrane is 3.68 km/s (Table 1 in Wang et al., 2013). The difference is about 2%. The average whole-crustal shear velocity for the Longmenshan where crystalline basement is exposed is 3.72 km/s. This velocity is derived by replacing the sediments by lower crust in the Songpan-Ganzi terrane model (Table 1 in Wang et al., 2013). Thus, the difference in average whole-crustal shear velocity between the Sichuan basin and the Longmenshan is about 3%. Using also the compressional velocities quoted in Table 1 of Wang et al. (2013), the pull-up/pull-down effect on the Moho using the different crustal velocity structures for the Sichuan basin, Longmenshan, and Songpan-Ganzi terrane has been estimated. This has been done by calculating the *Ps* conversion time for the Moho through one of the models and then, for the other models, adjusting the Moho depth to keep the *Ps* conversion time the same. It turns out that the estimated pull-up/pull-down effect on the Moho is a maximum of 2.5 km. This is somewhat less than the vertical box size of 6 km used in the migration, which effectively determines the vertical resolution in this study.

The negative phase above the Moho (N in Figures 3, 5, 6, and 8) always just increases smoothly and gradually in depth from SE to NW. In the four northeastern cross sections (Figures 5a–5d and 6a–6d), the phase is weaker directly beneath the surface trace of the YBF than it is under either the Sichuan basin or the Tibetan plateau. This may be due to the fact that it is, in fact, absent directly beneath the surface trace of the YBF and that the smoothing caused by the 24 km length of the migration box in the profile direction is responsible for the continuous but weaker appearance of the phase below the YBF. In this case, the origin of the phase under the Sichuan basin could be different to that under the Tibetan plateau and the similar depth at which the phase appears beneath the Sichuan basin and the Tibetan plateau could be a coincidence. To emphasize the opposite dip directions of the base of the Mesozoic sediments of the Sichuan basin and the negative phase, N, the data from the station JIULG are shown (Figure 8c) and can be compared to the data from the station GAUND (Figure 3a). The station JIULG is situated closer to the edge of the Sichuan basin than the station GAUND (Figure 1). In the summed trace at the top, the *Ps* conversion from the base of the Mesozoic sediments occurs at 1.25 s for JIULG compared to 1.48 s for GAUND, whereas the negative phase, N, occurs at a later time for JIULG (4.8 s) than for GAUND (4.6 s). However, as argued above, the negative phase, N, under the Sichuan basin southeast of the YBF is most probably, at least to a degree of about 50%, due to multiples from discontinuities in the upper crust, as opposed to a primary *Ps* conversion from the top of an LVZ at the base of the crust. In contrast to the Moho, the negative phase, N, above the Moho shows no step-like feature. Providing that northwest of the YBF, the negative phase, N, is a primary *Ps* conversion, as has already been proposed by Zhang et al. (2009), the basal crustal layer beneath the Tibetan plateau in the study area is a low velocity layer and is thickest just to the northwest of the Moho step. Assuming that the negative phase, N2 (Figures 3c, 5, 6, 8a, and 8b), is a primary *Ps* conversion, beneath the high Tibetan plateau the top of a midcrustal LVZ occurs at about 25 km depth.

In the depth domain images, the depth range between the Moho and the mantle transition zone is quite featureless except for a band of positive phases between 100 and 150 km depth (Figure 5). This band of positive phases possibly includes *PpPs* multiples from intracrustal boundaries at 30–35 km depth, and beneath the high Tibetan plateau, it could include the *PpSs* multiple of the negative *Ps* conversion, N2. The 410 and 660-km discontinuities bounding the mantle transition zone can also be recognized (Figures 5 and 7). They are best observed on the northeasternmost cross section (Figures 5a and 7a) where they both occur with a more or less constant amplitude across the whole cross section. In this cross section there is a slight tendency for both discontinuities to apparently occur at approximately 5-km shallower depths (i.e., 405 and 655 km) than usual. Toward the SW, on the other five cross sections, the discontinuities display, at face value, more variability in amplitude and structure, and there is also less of a tendency for them to occur at shallower depths than normal. This suggests that the velocity structure of the mantle beneath much of the array is similar to the IASP91 velocity model (Kennett & Engdahl, 1991). However, toward the NE end of the array, the two discontinuities appear to be about 5 km shallower. Alternatively, if the mantle velocity above the 410-km discontinuity is about 1.25% faster than the IASP91 velocity model (Kennett & Engdahl, 1991), then this could cause the observed apparent 5-km shallowing of both discontinuities. It is unlikely that

lateral variations in crustal structure cause the apparent difference, as even the difference in crustal structure between the Sichuan basin (~48-km-thick crust with average shear velocity of 3.6 km/s according to Wang et al., 2013) and the Songpan-Ganzi terrane (~65-km-thick crust with average shear velocity of 3.68 km/s according to Wang et al., 2013) only causes a difference in the *Ps* conversion time from the 410-km discontinuity of 0.1 s. The variability in amplitude and structure of the 410-km discontinuity includes a disruption in the strength of the conversion from this discontinuity beneath the Longmenshan fault zone on the three southwestern cross sections (Figures 5d–5f and 7d–7f) and slightly on the adjacent cross section to the NE (Figures 5c and 7c). These are the four cross sections (Figures 5c–5f) where the transition from the shallower Moho to the SE beneath the Sichuan basin to the deeper Moho to the NW beneath the Tibetan plateau occurs in an abrupt, step-like manner.

4. Discussion

There are several previous crustal-scale or even deeper cross sections across the Longmenshan fault zone based on either controlled-source or passive-source seismic experiments. Wang et al. (2007) completed an E-W controlled-source wide-angle seismic profile at 30°N. The cross section along this profile showed a deepening of the Moho by 15–20 km over about 45-km horizontal distance to the W of the Longmenshan fault zone. Wang et al. (2015) carried out a NW-SE controlled-source wide-angle seismic profile which crossed the Longmenshan fault zone at about 30.5°N. The cross section along this profile showed an approximately 45-km-thick crust below the Sichuan basin, thickening beneath the Longmenshan and the high Tibetan plateau to about 60 km about 100 km northwest of the Yingxiu-Beichuan fault (Figure 5f). However, it showed no step in or abrupt deepening of the Moho across the Longmenshan fault zone. This is perhaps somewhat surprising as the middle six shots along the profile were only spaced 20–25 km apart and thus should have been able to resolve a step or abrupt deepening in the Moho if such a structure exists. Wang et al. (2013) completed a NW-SE controlled-source wide-angle seismic profile which crossed the Longmenshan fault zone at about 31°N. The cross section along this profile showed a 50-km-thick crust beneath the Sichuan basin, thickening gradually beneath the Longmenshan and high Tibetan plateau (Figure 5d). It also showed no step in or abrupt deepening of the Moho across the Longmenshan fault zone. On the other hand, it may have been that the shots, which were spaced about 100 km apart, were not optimally placed to image an abrupt deepening of the Moho across the Longmenshan fault zone. Zhang et al. (2009, 2010) completed a NW-SE passive-source profile crossing the Longmenshan fault zone at about 31°N. A cross section based on receiver function analysis of the data showed a 15 to 20-km step in the Moho within 10 km to the NW of the Longmenshan fault zone (epicenter of Wenchuan earthquake, Figure 5d). Robert et al. (2010) completed a passive-source profile oriented W-E where it crossed the Longmenshan fault zone at about 31°N. A cross section based on receiver function analysis of the data showed an abrupt deepening of the Moho by 15–20 km over about 15 km horizontal distance about 40 km W of the surface trace of the YBF (Figure 5d). From an array of about 300 seismic stations in western Sichuan, Liu et al. (2014) presented an E-W cross section at 31°N based on receiver functions and surface wave tomography. This cross section showed a 25 to 30-km step in the Moho 25–30 km W of the surface trace of the Longmenshan fault zone (Figure 5d). Jia et al. (2014) carried out a NW-SE controlled-source wide-angle seismic profile which crossed the Longmenshan fault zone at about 31.4°N. The cross section along this profile showed a 40 to 45-km-thick crust under the Sichuan basin, thickening fairly gradually to 55–60 km under the high Tibetan plateau (Figure 5c). It also showed no step in or abrupt deepening of the Moho across the Longmenshan fault zone. Again, this is perhaps somewhat surprising as the middle nine shots along the profile were only spaced on average about 20 km apart and thus should have been able to resolve a step in or an abrupt deepening of the Moho if such a structure exists. The two cross sections of Guo et al. (2013) and Xu et al. (2016) are both from a NW-SE profile which crossed the Longmenshan fault zone at about 31.6°N. The model derived from the refraction/wide-angle reflection profile of Xu et al. (2016) revealed an approximately 40-km-thick crust beneath the Sichuan basin thickening gradually to about 60 km beneath the Songpan-Ganzi terrane of the high Tibetan plateau (Figure 5b). This model also showed no step in or abrupt deepening of the Moho across the Longmenshan fault zone. In this case it is not possible to appeal to the spacing of the shot-points to explain the lack of a step in or an abrupt deepening of the Moho across the Longmenshan fault zone, as the section from the near-vertical incidence reflection profile (Guo et al., 2013) showed a clear Moho all along the profile. Although not completely smooth, the maximum offset of the reflection from the Moho along the profile according to Guo et al. (2013) is of the

order of 5 km and not 15–30 km. In summary, the models derived from the controlled-source wide-angle profiles show a more gradual change in crustal thickness across the Longmenshan fault zone, whereas the images from the previous passive-source profiles show an abrupt change in crustal thickness or even a step in the Moho across the Longmenshan fault zone.

Two of the previous studies (Guo et al., 2013; Xu et al., 2016) show sections which cross the Longmenshan fault zone at about 31.6°N. The cross section in this study which incorporates data from the Longmenshan fault zone crossing at about 31.6°N is the second cross section, C-D (Figure 5b), from the NE. This cross section (Figure 5b) also shows a smooth, gradual deepening of the Moho to the NW from the Sichuan basin to the high Tibetan plateau, in agreement with the sections of Guo et al. (2013) and Xu et al. (2016). The study of Jia et al. (2014) crosses the Longmenshan fault zone at about 31.4°N. The cross section in this study which incorporates data from the Longmenshan fault zone crossing at about 31.4°N is the third cross section, E-F (Figure 5c), from the NE. Whereas this cross section shows a 20-km step in the Moho with an indication for an overlap of the deeper Moho from the NW below the shallower Moho from the SE, the cross section of Jia et al. (2014) shows a much more gradual deepening of the Moho toward the NW into the Tibetan plateau (Figure 5c). A further four of the previous studies show cross sections which cross the Longmenshan fault zone at about 31°N. The fourth cross section, G-H (Figure 5d), from the NE in this study crosses the Longmenshan fault zone at 31°N and also shows a 20-km step in the Moho, similar to those shown by the three previous passive-source studies. However, the step in the Moho shown in the cross section which crosses the Longmenshan fault zone at 31°N in this study is located further to the NW than those shown by the three previous passive-source studies which also cross the Longmenshan fault zone at 31°N. More specifically, it is located about 40 km NW of the surface trace of the Longmenshan fault zone and thus at least 5–10 km NW of the steps shown by the three previous passive-source studies (Figure 5d). On the other hand, the difference of 5–10 km is less than the 24 km length of the migration box in the direction perpendicular to the Longmenshan fault zone. Nevertheless, despite the range in distances NW of the Longmenshan fault zone at which the step in the Moho is reported by the three previous passive-source studies and this study, all of these studies report that the step in the Moho occurs to the NW of the Longmenshan fault zone and not SE of it. One of the previous studies (Wang et al., 2015) shows a cross section which crossed the Longmenshan fault zone at about 30.5°N. The southwesternmost cross section, M-N (Figure 5f), in this study crosses the Longmenshan fault zone at about 30.5°N and shows a 20-km step in the Moho with an indication for an overlap of the deeper Moho from the NW below the shallower Moho from the SE. In contrast, the cross section of Wang et al. (2015) shows a much more gradual deepening of the Moho toward the NW into the Tibetan plateau (Figure 5f).

Perhaps the most intriguing finding of this study is the NE to SW along-strike variation in the Moho structure across the Longmenshan fault zone. Along the two northeastern cross sections which cross the Longmenshan fault zone north of 31.5°N (Figures 6a and 6b), the Moho shows a smooth, gradual deepening to the NW from the Sichuan basin to the high Tibetan plateau. In contrast, along the four southwestern cross sections which cross the Longmenshan fault zone south of 31.5°N (Figures 6c–6f), there is an abrupt 20-km step in the Moho. Further, along the three cross sections E-F, K-L, and M-N (Figures 6c, 6e, and 6f), in addition to an abrupt 20-km step, there is some indication of an overlap of the deeper Moho from the NW below the shallower Moho from the SE. This derived structure of the Moho is shown in the 3-D model (Figure 9a) and simplified cartoon (Figure 9b) capturing the main elements of the Moho structure beneath the Longmenshan. The 3-D model and the simplified cartoon give a good impression of how the smooth change of Moho depths in the NE transforms to an abrupt step in the center and SW. They also give an impression of where overlap of the deeper Moho below the Tibetan plateau with the shallower Moho under the Sichuan basin seems to be occurring, although, as stated above, the size of the migration boxes may artificially exaggerate the overlap. The situation with overlap in the Moho is reminiscent of a similar structure having been identified along the INDEPTH IV profile crossing the Kunlun mountains in NE Tibet (Karplus et al., 2011; Mechie et al., 2012). The interpretation provided by Karplus et al. (2011) for NE Tibet was that lower crust from the Songpan-Ganzi terrane of the high Tibetan plateau was underthrusting or flowing northward beneath the Moho of the lower elevation Qaidam basin. Thus, the high Tibetan plateau may be thickening northward into south Qaidam as its weak, thickened lower crust is injected beneath stronger Qaidam crust. A similar situation could very well be occurring beneath three of the profiles presented in this study. In this case the high Tibetan plateau may be starting to thicken southeastward into the southwestern Sichuan basin as

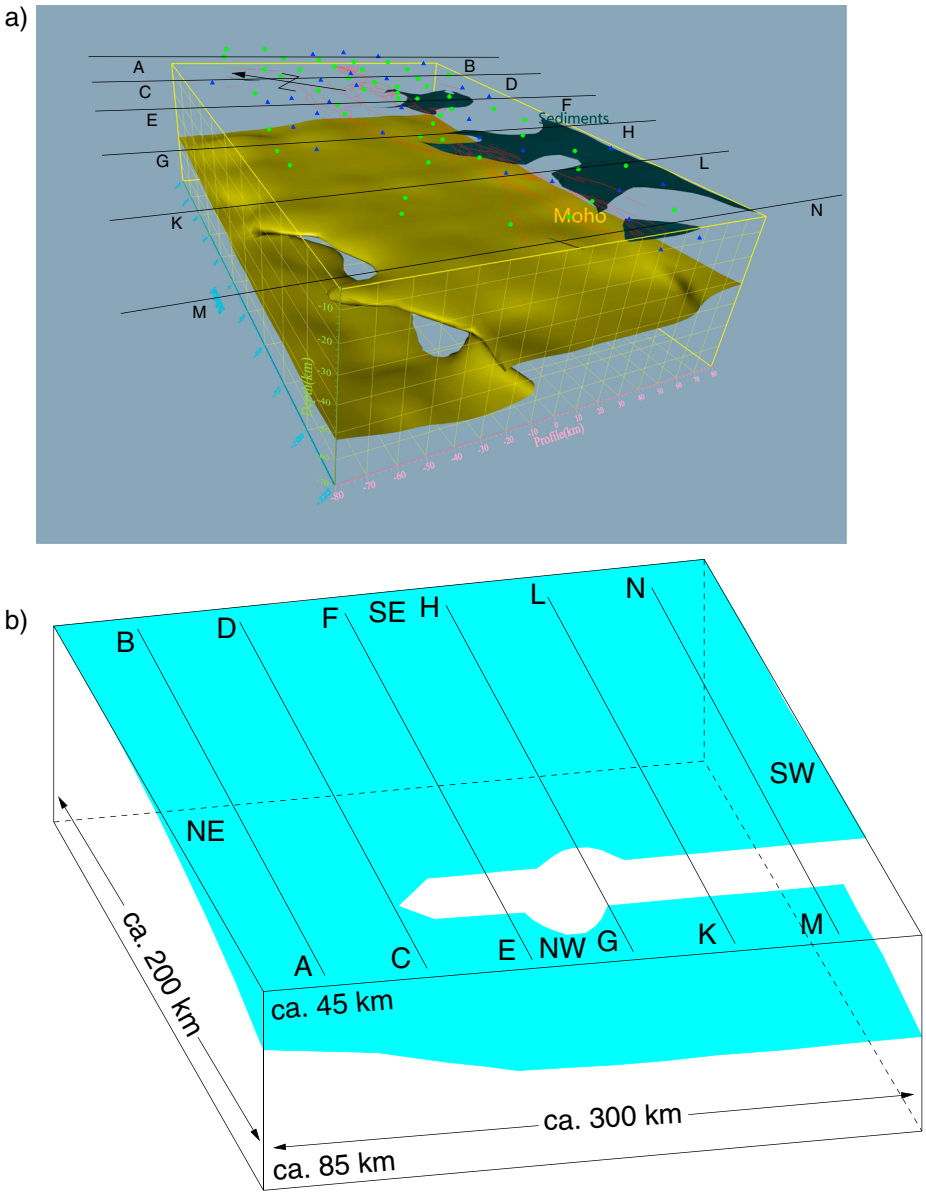

Figure 9. (a) Three-dimensional model showing the main elements of the Moho structure beneath the Longmenshan fault zone. The surfaces representing the Moho and the sediments of the Sichuan basin are marked. These surfaces have been drawn automatically once a threshold for the respective conversions has been defined. The seismic stations are marked by small blue triangles (Chinese stations) and small green circles (German stations). The faults in the Longmenshan are marked by red lines. The diagram shows in detail how the Moho is continuous in the northeast but broken and even overlapping in the centre and southwest. (b) Simplification of the 3-D model in Figure 9a, showing a cartoon of the Moho geometry from NE to SW along the Longmenshan. The depth range from ~45 to ~85 km is shown.

weak, thickened lower crust of the Songpan-Ganzi terrane is injected beneath the stronger crust of the Sichuan basin. Feng et al. (2014) show how this may occur in NE Tibet. Further to the north where there is no break in the Moho but rather just a steady increase in Moho depth in going from the Sichuan basin to the high Tibetan plateau, the lithosphere of the Sichuan basin may still be more successfully resisting the advance of the Tibetan plateau.

Observations of negative *Ps* conversions within the crust beneath the high Tibetan plateau, including the region of the high plateau covered in this study, are already known (Kind et al., 1996; Zhang et al., 2009, 2010). From the inversion of receiver function and Rayleigh wave phase velocity data and the modeling of the radial component of teleseismic *P* waveforms, Kind et al. (1996) found a low shear velocity zone

between about 20 and 40 km depth in the middle crust beneath southern Tibet north of the Indus-Yarlung suture. The top of this low shear velocity zone in southern Tibet has been interpreted as marking the top of a midcrustal partial melt layer as it spatially coincides with the top of a zone of high electrical conductivity and the occurrence of prominent near-vertical incidence seismic reflections (Nelson et al., 1996). A synoptic study of the midcrustal low shear velocity zone beneath Tibet (Yang et al., 2012) found significant low shear velocity features across most of the Tibetan middle crust at depths between 20 and 40 km and that these features are most prominent near the periphery of the plateau. In western and central Tibet the low shear velocity zone is coincident with strong midcrustal radial anisotropy (Shapiro et al., 2004; Yang et al., 2012). Thus, in addition to partial melt, aligned anisotropic minerals may be contributing to the cause of the midcrustal low shear velocity zone beneath Tibet (Yang et al., 2012). The negative *Ps* conversion from about 25 km depth beneath the high Tibetan plateau observed in this study (N2 in Figures 3c, 5, 6, 8a, and 8b) is interpreted as being the local representative of the top of the Tibetan midcrustal low shear velocity zone in this area. The deeper negative *Ps* conversion beneath the high Tibetan plateau observed in this study (N in Figures 3c, 5, 6, and 8b) has also been observed by Zhang et al. (2009) and interpreted by these authors as being due to the top of an LVZ possibly involving high temperatures, fluids, and/or partial melts. The fact that the top of the basal crustal layer beneath the Tibetan plateau, northwest of the YBF, appears to be smooth and undeformed (Figures 5 and 6) means that there is a rapid change in thickness of this layer where the Moho shows abrupt changes in depth. The basal crustal layer is thickest just northwest of the location where the abrupt deepening of the Moho occurs. If the low velocity, basal crustal layer transitions from being strong southeast of the northwestern edge of the shallower Moho to being weak, as discussed above, to the northwest beneath the Songpan-Ganzi terrane of the high Tibetan plateau, then this would be compatible with the top of this layer being smooth and undeformed to the northwest of the YBF.

What is somewhat surprising is that a boundary associated with a negative phase also seems to occur beneath the Sichuan basin just above the Moho. Even if this negative phase is only in part due to a primary *Ps* conversion, then it indicates the presence of a low velocity layer at the base of the crust beneath the Sichuan basin. Neither the controlled-source studies of Wang et al. (2007), Wang et al. (2013), Jia et al. (2014), Wang et al. (2015), and Xu et al. (2016) nor the passive-source study of Liu et al. (2014) showed any indication of a deep crustal low velocity layer beneath the Sichuan basin. However, controlled-source experiments may not always recognize LVZs in the deeper crust (see e.g., Zhao et al., 2001 for a discussion on this point). On the other hand, the passive-source studies of Robert et al. (2010) and Zhang et al. (2009, 2010) did show some indications, although not as prominent as in this study, of a negative phase from the deep crust beneath the Sichuan basin. However, neither Robert et al. (2010) nor Zhang et al. (2009, 2010) chose to interpret the indications for this negative phase in their data. As argued above, the negative phase, N, under the Sichuan basin is most probably, at least to a degree of about 50%, due to multiples from discontinuities in the upper crust, as opposed to a primary *Ps* conversion from the top of a basal crustal LVZ. Beneath the Sichuan basin the difference in delay times between the negative phase, N, and the positive *Ps* conversion from the Moho is about 1 s (Figures 3a and 8c). If the negative phase, N, is partly due to a primary *Ps* conversion, then the thickness of the low velocity layer at the base of the crust is about 10 km.

With respect to the depth range between the Moho and the mantle transition zone, the region between 200 km depth and the top of the mantle transition zone is quite featureless in agreement with Zhang et al. (2010). In contrast to Zhang et al. (2010), in the present study, a band of positive phases occurs between 100 and 150 km depth and there is no evidence for the lithosphere-asthenosphere boundary (Figure 5). The profile of Zhang et al. (2009, 2010) extends as far west as 101.5°E. The 410-km discontinuity below this profile is depressed below eastern Tibet by about 30 km with respect to the Sichuan basin, whereas the 660-km discontinuity remains at nearly the same depth beneath the whole profile (Zhang et al., 2010). Although the cross section which crosses the Longmenshan fault zone at 31°N in this study (Figures 5d and 7d) does not extend much further west than 103°E, it shows no indication of the 410-km discontinuity deepening toward the NW end of the profile. At 103°E, the image of Zhang et al. (2010) already shows the 410-km discontinuity to be at 420-km depth. The disruption in the strength of the conversion from the 410-km discontinuity seen in the image of Zhang et al. (2010) beneath the Longmenshan fault zone can also be observed on the cross section which crosses the Longmenshan fault zone at 31°N in this study (Figure 5d). It is also present in the image derived using the bootstrap technique (Figure 7d), although shifted somewhat to the SW. This disruption can also be observed on the two cross sections to the SW (Figures 5e, 5f, 7e, and 7f)

and slightly on the adjacent cross section to the NE (Figures 5c and 7c). Whether this disruption is apparent due to complex structure at shallower levels or whether it is real due to a disruption in the 410-km discontinuity remains uncertain. However, it is perhaps interesting that the disruption occurs on the four cross sections in which the Moho deepens abruptly from the Sichuan basin to the high Tibetan plateau (Figures 5c–5f), while it is absent in the two northeasternmost cross sections where the Moho deepens gradually across the Longmenshan fault zone (Figures 5a and 5b). If the disruption is real, then it could be due to shortened, thickened upper mantle material becoming unstable and sinking and impinging on the 410-km discontinuity beneath the boundary between the Tibetan plateau and the Sichuan basin as modeled by Houseman et al. (1981). It is possible that this process is not so far advanced, and thus, no disruption is observable below the two northeasternmost cross sections. The average depth of the 660-km discontinuity along the cross section which crosses the Longmenshan fault zone at 31°N in this study is 660 km, which is about 10 km shallower than in the image of Zhang et al. (2010). The disruption in the strength of the conversion from the 660-km discontinuity seen in the image of Zhang et al. (2010) beneath the Longmenshan fault zone is not observed on the cross section which crosses the Longmenshan fault zone at 31°N in this study (Figure 5d).

5. Conclusions

Seismic imaging using *P* receiver functions along six profiles across the Longmenshan fault zone reveals the deep structure in the region of the epicenter of the Wenchuan earthquake. Positive *Ps* conversions originating from 5 to 10 km depth indicate the base of the Mesozoic sediments in the Sichuan basin and the base of the flysch deposits in the Songpan-Ganzi terrane. The Moho is also recognized as a prominent positive *Ps* conversion. It deepens from 40–50 km depth in the SE beneath the Sichuan basin to 55–70 km depth in the NW under the Songpan-Ganzi terrane of the high Tibetan plateau. The variable character of the Moho deepening along the trend of the Longmenshan fault zone is one of the important findings of this study. In the NE of the study region the deepening is smooth, whereas in the middle and SW the deepening is abrupt with, in some cases, in addition to abrupt deepening indications, seemingly, for a Moho overlap (Figures 5, 6, and 9). These results are in broad agreement with the results from previous passive-source profiles which cross the Longmenshan fault zone at 31°N and previous controlled-source profiles which cross the Longmenshan fault zone at 31.6°N. However, they are not in agreement with the results from previous controlled-source profiles which cross the Longmenshan fault zone at 30.5°N, 31°N, and 31.4°N. A negative *Ps* conversion from the top of a midcrustal LVZ at about 25 km depth is found at stations in the Songpan-Ganzi terrane of the high Tibetan plateau. This conversion is interpreted to represent the top of the Tibetan midcrustal low shear velocity zone in the study region, being due to partial melt and/or aligned anisotropic minerals. Beneath the Sichuan basin, a negative phase about 1 s earlier than the Moho *Ps* conversion is, to a large extent, almost certainly due to multiples from discontinuities in the upper crust. However, to a lesser extent, it may also be due to a *Ps* conversion from the top of a low velocity layer at the base of the crust about 10 km above the Moho. Northwest of the YBF, the major fault of the Longmenshan fault zone in the study region, a further negative *Ps* conversion originates from the top of a low velocity layer in the lower crust beneath the Tibetan plateau. In contrast to the Moho, the top of this low velocity layer shows a smooth deepening from SE to NW. This leads to abrupt thickness changes of the basal crustal, low velocity layer with the layer being thickest just NW of the abrupt deepening of the Moho. If the basal crustal, low velocity layer transitions from being strong to the southeast of the northwestern edge of the shallower Moho to being weak to the northwest beneath the high Tibetan plateau, then this would be compatible with the top of this layer showing a smooth deepening from SE to NW. The lower crustal and Moho structure along three of the four southwestern profiles in the study region is reminiscent of a similar structure beneath the southern margin of the Qaidam basin in NE Tibet just N of the Kunlun mountains (Karplus et al., 2011; Mechie et al., 2012). At greater depths, positive *Ps* conversions can be observed from the 410 and 660-km discontinuities at the top and bottom of the mantle transition zone, respectively. There is a disruption in the strength of the conversion from the 410-km discontinuity beneath the Longmenshan fault zone in the four southwestern cross sections in which the Moho deepens abruptly from the Sichuan basin to the high Tibetan plateau (Figures 5c–5f). If real, then this disruption could be due to shortened, thickened, and thus unstable upper mantle material sinking and impinging on the 410-km discontinuity below the boundary between the Tibetan plateau and the Sichuan basin (Houseman et al., 1981).

Acknowledgments
The fieldwork was part of the project "Deep geological survey of the structural belt along the Longmenshan," financed through the Chinese Geological Survey (CGS) by the Ministry of Science and Technology of China (grant 121201122026[3-5]). The Beijing Gangzhen Corp. Limited is thanked for providing the Chinese instruments for the fieldwork, while the Geophysical Instrument Pool of the Deutsches GeoForschungsZentrum Potsdam (GFZ) is acknowledged for providing the German instruments. The data from the 50 German instruments (FDSN code 2F 2012-2013) are archived at the GEOFON data center (Qian & Mechie, 2012). These data are publicly available. The data from the 30 Chinese stations are archived in China. Permission to use these data should be sought through H.Q. from the Chinese Geological Survey. The Sichuan Province Land Resource Institute is thanked for providing support for the work as are the local people who guarded the instruments during the fieldwork.

References

Ammon, C. J., Randall, C. E., & Zandt, G. (1990). On the nonuniqueness of receiver function inversion. *Journal of Geophysical Research*, *95*, 15,303–15,318. https://doi.org/10.1029/JB095iB10p15303

Coleman, T. F., & Li, Y. (1994). On the convergence of interior-reflective Newton methods for nonlinear minimization subject to bounds. *Mathematical Programming*, *67*(1-3), 189–224. https://doi.org/10.1007/BF01582221

Cook, K. L., Royden, L. H., Burchfiel, B. C., Lee, Y.-H., & Tan, X. (2013). Constraints on Cenozoic tectonics in the southwestern Longmen Shan from low-temperature thermochronology. *Lithosphere*, *5*(4), 393–406. https://doi.org/10.1130/L263.1.10.1130/L263.1

Dueker, K. G., & Sheehan, A. F. (1997). Mantle discontinuity structure from midpoint stacks of converted P to S waves across the Yellowstone hotspot track. *Journal of Geophysical Research*, *102*, 8313–8327. https://doi.org/10.1029/96JB03857

Dueker, K. G., & Sheehan, A. F. (1998). Mantle discontinuity structure beneath the Colorado Rocky Mountains and High Plains. *Journal of Geophysical Research*, *103*, 7153–7169. https://doi.org/10.1029/97JB03509

Feng, M., Kumar, P., Mechie, J., Zhao, W., Kind, R., Su, H., et al. (2014). Structure of the crust and mantle down to 700 km depth beneath the east Qaidam basin and Qilian Shan from P and S receiver functions. *Geophysical Journal International*, *199*, 1416–1429. https://doi.org/10.1093/gji/ggu335

Guo, X., Gao, R., Keller, G. R., Xu, X., Wang, H., & Li, W. (2013). Imaging the crustal structure beneath the eastern Tibetan plateau and implications for the uplift of the Longmen Shan range. *Earth and Planetary Science Letters*, *379*, 72–80. https://doi.org/10.1016/j.epsl.2013.08.005

Herrmann, R. B., & Ammon, C.J. (2002). Surface waves, receiver functions and crustal structure. Computer Programs in Seismology. Retrieved from http://www.eas.slu.edu/eqc/eqccps.html

Houseman, G. A., McKenzie, D. P., & Molnar, P. (1981). Convective instability of a thickened boundary layer and its relevance for the thermal evolution of continental convergent belts. *Journal of Geophysical Research*, *86*, 6115–6132. https://doi.org/10.1029/JB086iB07p06115

Jia, S. X., Liu, B. J., Xu, Z. F., Liu, Z., Feng, S. Y., Zhang, J. S., et al. (2014). The crustal structures of the central Longmenshan along and its margins as related to the seismotectonics of the 2008 Wenchuan earthquake. *Science China: Earth Sciences*, *57*(4), 777–790. https://doi.org/10.1007/s11430-013-4744-9

Karplus, M. S., Zhao, W., Klemperer, S. L., Wu, Z., Mechie, J., Shi, D., et al. (2011). Injection of Tibetan crust beneath the south Qaidam Basin: Evidence from INDEPTH IV wide-angle seismic data. *Journal of Geophysical Research*, *116*, B07301. https://doi.org/10.1029/2010JB007911

Kennett, B. L. N., & Engdahl, E. R. (1991). Traveltimes for global earthquake location and phase identification. *Geophysical Journal International*, *105*(2), 429–465. https://doi.org/10.1111/j.1365-246X.1991.tb06724.x

Kind, R., Kosarev, G. L., & Petersen, N. V. (1995). Receiver functions at the stations of the German Regional Seismic Network (GRSN). *Geophysical Journal International*, *121*(1), 191–202. https://doi.org/10.1111/j.1365-246X.1995.tb03520.x

Kind, R., Ni, J., Zhao, W., Wu, J., Yuan, X., Zhao, L., et al. (1996). Evidence from earthquake data for a partially molten crustal layer in southern Tibet. *Science*, *274*(5293), 1692–1694. https://doi.org/10.1126/science.274.5293.1692

Kind, R., Yuan, X., & Kumar, P. (2012). Seismic receiver functions and the lithosphere-asthenosphere boundary. *Tectonophysics*, *536-537*, 25–43. https://doi.org/10.1016/j.tecto.%202012.03.005

Kumar, P., Yuan, X., Kind, R., & Ni, J. (2006). Imaging the colliding Indian and Asian lithospheric plates beneath Tibet. *Journal of Geophysical Research*, *111*, B06308. https://doi.org/10.1029/2005JB003930

Langston, C. A. (1979). Structure under Mount Rainier,Washington, inferred from teleseismic body waves. *Journal of Geophysical Research*, *84*, 4749–4762. https://doi.org/10.1029/JB084iB09p04749

Li, H., Wang, H., Xu, Z., Si, J., Pei, J., Li, T., et al. (2013). Characteristics of the fault-related rocks, fault zones and the principal slip zone in the Wenchuan Earthquake Fault Scientific Drilling Project Hole-1 (WFSD-1). *Tectonophysics*, *584*, 23–42. https://doi.org/10.1016/j.tecto.%202012.08.021

Liu, Q. Y., van der Hilst, R. D., Li, Y., Yao, H. J., Chen, J. H., Guo, B., et al. (2014). Eastward expansion of the Tibetan plateau by crustal flow and strain partitioning across faults. *Nature Geoscience*, *7*(5), 361–365. https://doi.org/10.1038/ngeo2130

Mechie, J., Zhao, W., Karplus, M. S., Wu, Z., Meissner, R., Shi, D., et al. (2012). Crustal shear (S) velocity and Poisson's ratio structure along the INDEPTH IV profile in Northeast Tibet as derived from wide-angle seismic data. *Geophysical Journal International*, *191*(2), 369–384. https://doi.org/10.1111/j.1365-246X.2012.05616.x

Müller, G. (1985). The reflectivity method: A tutorial. *Journal of Geophysics*, *58*, 153–174.

Nelson, K. D., Zhao, W., Brown, L. D., Kuo, J., Che, J., Liu, X., et al. (1996). Partially molten middle crust beneath southern Tibet: Synthesis of project INDEPTH results. *Science*, *274*(5293), 1684–1688. https://doi.org/10.1126/science.274.5293.1684

Owens, T. J., Zandt, G., & Taylor, S. R. (1984). Seismic evidence for an ancient rift beneath the Cumberland Plateau, Tennessee: A detailed analysis of broadband teleseismic P waveforms. *Journal of Geophysical Research*, *89*, 7783–7795. https://doi.org/10.1029/JB089iB09p07783

Qian, H., & Mechie, J. (2012). Temporary seismological network in Longmenshan, China (2012/2013). Deutsches GeoForschungsZentrum GFZ. Other/Seismic Network. https://doi.org/10.14470/7S7567431325

Qian, H., Mechie, J., Li, H., Xue, G., Su, H., & Cui, X. (2016). An approach to jointly invert hypocenters and 1-D velocity structure and its application to the Lushan earthquake series. *Journal of Seismology*, *20*(1), 213–232. https://doi.org/10.1007/s10950-015-9521-0

Robert, A., Zhu, J., Vergne, J., Cattin, R., Chan, L. S., Wittlinger, G., et al. (2010). Crustal structures in the area of the 2008 Sichuan earthquake from seismologic and gravimetric data. *Tectonophysics*, *491*(1-4), 205–210. https://doi.org/10.1016/j.tecto.%202009.11.010

Sacchi, M. D. (1998). A bootstrap procedure for high-resolution velocity analysis. *Geophysics*, *63*(5), 1716–1725. https://doi.org/10.1190/1.1444467

Schulte-Pelkum, V., & Mahan, K. H. (2014). A method for mapping crustal deformation and anisotropy with receiver functions and first results from USArray. *Earth and Planetary Science Letters*, *402*, 221–233. https://doi.org/10.1016/j.epsl.2014.01.050

Shapiro, N. M., Ritzwoller, M. H., Molnar, P., & Levin, V. (2004). Thinning and flow of Tibetan crust constrained by seismic anisotropy. *Science*, *305*(5681), 233–236. https://doi.org/10.1126/science.1098276

Sheriff, R. E., & Geldart, L. P. (1995). *Exploration seismology* (p. 592). Cambridge: Cambridge University Press. https://doi.org/10.1017/CBO9781139168359

Vinnik, L. P. (1977). Detection of waves converted from P to SV in the mantle. *Physics of the Earth and Planetary Interiors*, *15*(1), 39–45. https://doi.org/10.1016/0031-9201(77)90008-5

Wang, C. Y., Han, W. B., Wu, J. P., Lou, H., & Chan, W. W. (2007). Crustal structure beneath the eastern margin of the Tibetan plateau and its tectonic implications. *Journal of Geophysical Research*, *112*, B07307. https://doi.org/10.1029/2005JB003873

Wang, M., Hubbard, J., Plesch, A., Shaw, J. H., & Wang, L. (2016). Three-dimensional seismic velocity structure in the Sichuan basin, China. *Journal of Geophysical Research: Solid Earth*, *121*, 1007–1022. https://doi.org/10.1002/2015JB012644

Wang, Y., Mooney, W. D., Yuan, X., & Okaya, N. (2013). Crustal structure of the northeastern Tibetan plateau from the southern Tarim Basin to the Sichuan Basin, China. *Tectonophysics*, *584*, 191–208. https://doi.org/10.1016/j.tecto.%202012.09.003

Wang, S.-J., Wang, F.-Y., Zhang, J.-S., Liu, B.-F., Zhang, C.-K., Zhao, J.-R., et al. (2015). A study of deep seismogenic environment in Lushan Ms7.0 earthquake zone by wide-angle seismic reflection/refraction profile. *Chinese Journal of Geophysics*, *58*, 474–485.

Weislogel, A. (2008). Tectonostratigraphic and geochronologic constraints on evolution of the northeast Paleotethys from the Songpan-Ganzi complex, Central China. *Tectonophysics*, *451*(1-4), 331–345. https://doi.org/10.1016/j.tecto.%202007.11.053

Xu, X., Keller, G. R., Gao, R., Guo, X., & Zhu, X. (2016). Uplift of the Longmen Shan area in the eastern Tibetan plateau: An integrated geophysical and geodynamic analysis. *International Geology Review*, *58*(1), 14–31. https://doi.org/10.1080/00206814,2015.1055595

Yang, Y., Ritzwoller, M. H., Zheng, Y., Shen, W., Levshin, A. L., & Xie, Z. (2012). A synoptic view of the distribution and connectivity of the mid-crustal low velocity zone beneath Tibet. *Journal of Geophysical Research*, *117*, B04303. https://doi.org/10.1029/2011JB008810

Yilmaz, Ö. (1987). Seismic Data Processing. Investigations in Geophysics (526 pp.). Society of Exploration Geophysicists, Tulsa.

Yuan, X. (2000). Teleseismic receiver function study and its application in Tibet and the Central Andes. PhD thesis, FU Berlin, Scientific Technical Report/GeoForschungsZentrum Potsdam STR00/10.

Yuan, X., Ni, J., Kind, R., Mechie, J., & Sandvol, E. (1997). Lithospheric and upper mantle structure of southern Tibet from a seismological passive source experiment. *Journal of Geophysical Research*, *102*, 27,491–27,500. https://doi.org/10.1029/97JB02379

Zhang, P.-Z., Shen, Z., Wang, M., Gan, W., Bürgmann, R., Molnar, P., et al. (2004). Continuous deformation of the Tibetan plateau from Global Positioning System data. *Geology*, *32*(9), 809–812. https://doi.org/10.1130/G20554.1

Zhang, Z., Wang, Y., Chen, Y., Houseman, G. A., Tian, X., Wang, E., & Teng, J. (2009). Crustal structure across Longmenshan fault belt from passive source seismic profiling. *Geophysical Research Letters*, *36*, L17310. https://doi.org/10.1029/2009GL039580

Zhang, Z., Yuan, X., Chen, Y., Tian, X., Kind, R., Li, X., & Teng, J. (2010). Seismic signature of the collision between the east Tibetan escape flow and the Sichuan Basin. *Earth and Planetary Science Letters*, *292*, 254–264. https://doi.org/10.1016/j.epsl.2010.01.046

Zhao, W., Mechie, J., Brown, L. D., Guo, J., Haines, S., Hearn, T., et al. (2001). Crustal structure of Central Tibet as derived from project INDEPTH wide-angle seismic data. *Geophysical Journal International*, *145*(2), 486–498. https://doi.org/10.1046/j.0956-540x.2001.01402.x